Radiat Environ Biophys (1994) 33:91–109

Radiation and Environmental Biophysics

Calculations of heavy-ion track structure

M. Krämer, G. Kraft

Gesellschaft für Schwerionenforschung, Biophysik, Max Planck-Strasse 1, D-64291 Darmstadt, Germany

Received: 23 September 1993 / Accepted in revised form: 17 January 1994

Abstract. A Monte Carlo model is presented to study details of the energy deposition inside tracks of heavy charged particles in water vapor. The input data for most of the calculations based on the binary encounter approximation are double-differential cross sections for electron emission after heavy-ion impact. The paths of the liberated electrons are simulated, taking into account elastic scattering, ionization, and excitation. Each basic interaction of an electron or heavy ion is treated individually. Radial dose distributions and specific energy deposition are calculated for projectiles from protons to uranium in the energy range from one to several hundred megaelectron volts per unified atomic mass unit. Good agreement with measurements in tissue-equivalent gas and propane is obtained for light and medium-heavy projectiles, whereas for heavy projectiles such as uranium, deviations around a factor of 2–3 are observed.

Introduction

Motivation

Experiments with beams of heavy charged particles have demonstrated that the biological response to heavy ions differs from sparsely ionizing radiation at all levels of biological organization. From experiments it is evident that both the nature of the biological lesion and the dose required to produce the lesion depend on the track structure [1, 19]. First, the efficiency of double-strand-break induction depends on both linear energy transfer (LET) and particle energy. Moreover, even in cases where the induction of double-strand breaks is strictly proportional to the dose, a significant prolongation for rejoining has been found [16].

Correspondence to: M. Krämer

Two major approaches are used to describe a heavy-ion track: the microdosimetry and the track structure model.

In microdosimetry [26], the energy deposition in a volume of approximately 1 μm in diameter is regarded to be the critical parameter. The measurements of the specific energy deposited in such a volume have shown a significant decrease of the mean values for increasing distance from the center. However, for large distances the mean specific energy deposition is constant, and the probability to hit the volume diminishes.

In the so-called track structure model there is no microstructure of the dose deposition. A continuous dose distribution inside the track is approximated by an r^{-2} dependence, where r is the distance from the center of the track. A modification is the core-penumbra model [10, 11], where a core of increased dose in the center of the track receives half the total energy lost by the heavy ion. An earlier variant of the model [9] cuts off the dose profile at small distances without a region of enhanced energy deposition in the center.

A realistic description of the particle track has to be compared with both approaches and should reproduce the measured radial dose distributions as well as the specific energy as a function of radial distance [34]. The preferred strategy to study details of track structure, spatial ionization and dose distributions is the Monte Carlo (MC) method. It has been used, for example, by Paretzke and Berger [25] to simulate the interaction of electrons and protons with water. The main purpose of the present work was to apply the MC technique to heavy ions in order to obtain dose distributions and specific energy as a function of the radial distance.

Calculation strategy

The calculation procedure using the MC method is designed to simulate the emission and transport of δ electrons after heavy-ion impact. The starting point is the creation of primary electrons along the path of a heavy ion. Each ionizing collision of a heavy ion with a molecule is treated individually, with a mean free path between two interactions according to the total cross section for this process. The emission angle and energy of a primary electron are sampled from the appropriate double-differential cross section. The mean kinetic energy of the created electrons is on the order of 100 eV. The maximum energy is determined by the binary collision kinematics between the projectile ion and a target electron, e.g., $\approx$20 keV for a 10-MeV/u ion. In this energy region an electron undergoes a few hundred to a few thousand collisions with atoms or molecules until its energy drops below a threshold where further ionization and, in consequence, biological damage is no longer possible.

The outline of the electron transport program presented here follows to some extent the instructions given by various authors [5, 14, 25]. The details of the basic interactions for electron transport used in our model are simpler than those discussed by Paretzke [24]. This simplified treatment is considered to be sufficient because the dominating uncertainties are the inaccurately known primary cross section for δ-electron creation by heavy ions. Each collision of an electron with a molecule is treated individually, taking into account three basic interactions: elastic scattering, ionization, and excitation. The single-collision approach is in contrast to high-energy simulations where multiple scatter-

ing distributions are used to combine the hundreds of thousands of interactions to a few hundred steps in a condensed random walk [5].

In the present calculation as well as in the cited experiments, the stopping material is a gas (water vapor and tissue-equivalent gas or propane), so that no solid state our plasmon effects are included. The mean free paths of the particles are calculated assuming the normal bulk density $\rho = 1$ g/cm^3. An essential requirement for any MC calculation is the precise knowledge of the underlying interaction cross sections. Though scarce, experimental data are used as far as possible for the construction of cross-section tables, either directly or via semiempirical fits.

The present model is restricted to electrons with energies above 10 eV. This is reasonable, because electrons of lower energies are below the ionization threshold of most molecules so that they produce little damage. Therefore, electrons are removed from the calculational procedure when their energy drops below 10 eV.

Transport of low-energy electrons in matter

Basic interactions

Cross sections for the basic processes of elastic scattering, excitation, and ionization are strongly energy dependent. Since the mean energy of the primary δ electrons is of the order of 100 eV, the cross sections for this particular energy region are of great importance. Figure 1 shows the cross sections used in the code, together with some experimental data. In the high-energy limit, the inelastic cross sections obey [7]

$$\sigma_{\text{inel}} = \frac{4\pi a_0^2 R}{T'} M_{\text{inel}}^2 \ln\left(\frac{T'}{c_{\text{inel}}}\right) \tag{1}$$

with

$$T' = \tfrac{1}{2} m_e v^2 \tag{2}$$

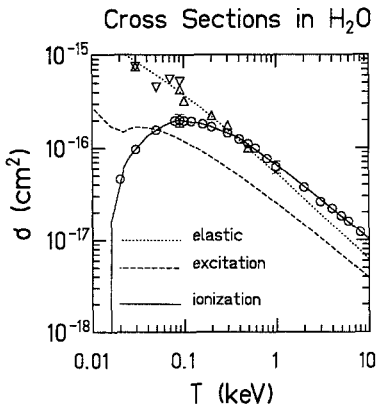

Fig. 1. The three basic cross sections for electrons in water vapor as function of electron energy. The *symbols* are experimental data (△ [18]; ▽ [39]; ○ [29]); the *curves* represent the cross sections used in this work

where $a_0 = 0.529 \times 10^{-8}$ cm is the Bohr radius, $R = 13.6$ eV is the Rydberg energy, M^2_{inel} is the oscillator strength, and c_{inel} is a constant with a value close to the interaction threshold.

Elastic scattering

Although elastic scattering does not contribute to energy dissipation, proper treatment is important because it is mainly responsible for the spatial diffusion of electrons in matter. Below 200 eV it is the dominating interaction. The handle elastic scattering, both the total cross section σ_{el} and the differential cross section $\mathrm{d}\sigma/\mathrm{d}\Omega$ are needed. Few experimental data on H_2O are available in the literature [18, 39]. Fortunately, it turns out that the differential as well as the total cross sections follow the additivity rule approximately:

$$\sigma_{H_2O} = \sigma_{H_2} + \tfrac{1}{2}\sigma_{O_2} \tag{3}$$

so that cross sections for H_2O can be synthesized from H_2 and O_2 data at energies where no water data are available. Two regimens of energy are distinguished to account for the deviations from Rutherford scattering at low energies. For high energies, $T > 0.5$ keV, the well-known Rutherford cross section with screening correction [5, 14, 21] is applied. For energies below 0.5 keV, the elastic-scattering cross section starts to deviate strongly from the Rutherford cross sections. Backward scattering in a single collision becomes increasingly important for decreasing electron energy. Therefore, experimental data are preferred rather than theoretical considerations. The few available data were fitted with a function of the form:

$$\frac{\mathrm{d}\sigma}{\mathrm{d}\Omega} = \frac{p_1}{4\pi}\left[p_2 + \frac{1}{p_0(2+p_0)}\right]^{-1}\left[(1-x+p_0)^{-2} + p_2 P_0 + p_3 P_2(x)\right] \tag{4}$$

The first term in the second set of brackets corresponds to the screened Rutherford cross section, with $p_0 = 2\eta$, $p_1 = \sigma_{\text{el}}$, the total elastic cross section. The factor in the first set of brackets ensures normalization to σ_{el}. P_0 and P_2 are the Legendre polynomials:

$$P_0 = 1, \quad P_2 = \tfrac{1}{2}(3x^2 - 1), \quad x = \cos(\theta) \tag{5}$$

introduced to describe the backscattering, its relative importance controlled by parameters p_2 and p_3. Equation 4 gives the best fit to the experimental distributions. Figure 2 shows the experimental data along with curves calculated from (4) and according to Rutherford scattering with screening correction.

Electronic excitation

Very little information is found in the literature on the energy dependence and angular distribution of electronic excitation processes in water vapor. From other molecules, e.g., N_2, it is known that the angular distribution of electrons after exciting molecular levels is strongly peaked forward [39]. Therefore, it is justified to assume that no change in the direction of flight of the incident electron takes place during excitation.

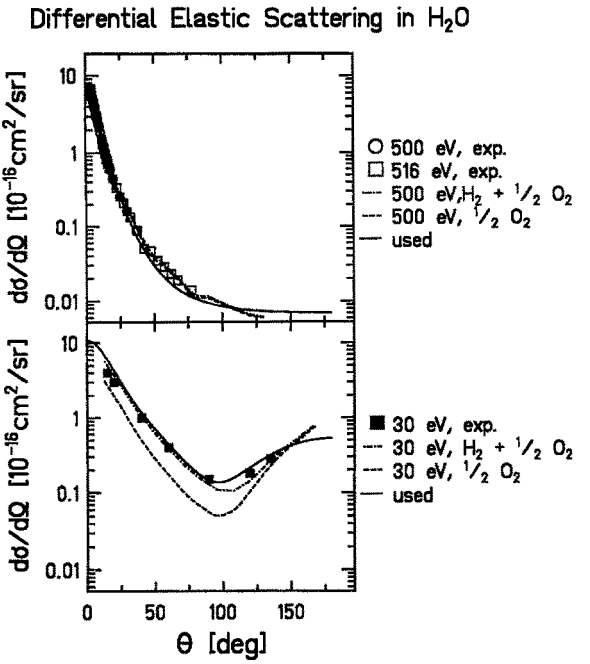

Fig. 2. Differential elastic scattering cross sections for electrons in water at two energies. Symbols show experimental data from Ref. 39. The *broken curves* demonstrate the additivity rule applied to experimental H_2 and O_2 data. The *solid curves* represent the fitted distributions

The mean energy $\langle k \rangle_{\text{exc}}$ transferred in excitation events is taken from Paretzke and Berger [25]. It is only weakly dependent on electron energy T and rises from 8 to about 13 eV in the energy range between 0.010 and 100 keV. Other molecules show similar dependences: N_2 from 7 to 13 eV, O_2 from 5.6 to 8.4 eV [14]. The dependence for H_2O can be parameterized as

$$\langle k \rangle_{\text{exc}}[\text{eV}] = \begin{cases} 8 + 5 \lg(100\,T), & T < 0.1 \text{ keV} \\ 13, & T > 0.1 \text{ keV} \end{cases}$$

The total electronic excitation cross section was taken from [25] and was parameterized according to (1) with the oscillator strength $M^2_{\text{exc}} = 1.194$ and the constant $c_{\text{exc}} = 8.2$ eV.

Ionization

When an ionization event occurs, a secondary electron is released from the molecule that is struck provided the energy of the primary electron is above the ionization threshold E_{ion}. This threshold equals the mean energy transfer $\langle k \rangle_{\text{ion}}$ needed to remove an electron from any shell of the H_2O molecule. The mean potential energy transfer for ionization rises from 12.7 to about 16.7 eV in the energy range between 0.0127 and 100 keV [25]. In the present calculations,

no attempt was made to resolve the partial ionization of one of the five shells of H_2O. Instead, for $\langle k \rangle_{ion}$ the empirical formulas (T in eV)

$$\langle k \rangle_{ion}[\text{eV}] = \begin{cases} 12.7 + 0.3 \ln(T/12.7)/\ln(20/12.7), & T \leq 20 \text{ eV} \\ 13.0 + 1.7 \ln(T/20.0)/\ln(1.25), & 20 \text{ eV} \leq T \leq 25 \text{ eV} \\ 14.7 + 2.0 \ln(T/25.0)/\ln(40.0), & T \geq 25 \text{ eV} \end{cases}$$

were constructed from the curve given in [25].

The total ionization cross section was derived from the experimental data published in Schutten et al. [29]. For energies greater than 0.3 keV, (1) gives a good fit to the experimental data with the oscillator strength $M_{ion}^2 = 3.14$ and the constant $c_{ion} = 12.7$ eV. For energies below 0.3 keV the experimental values are taken directly.

The energy and angular dependence of the double-differential cross sections of primary and secondary electrons, $d^2\sigma/dT\,d\Omega$, are difficult to handle, partly due to the lack of experimental data and partly because no analytical expressions or semiempirical relations are available from theory. An extensive data compilation exists for various materials and secondary electrons below 200 eV [23].

The energy differential cross section $d\sigma/dT_{sec}$ is needed to produce a random sample of secondary electron energies T_{sec}. It is described semiempirically by

$$\frac{d\sigma}{dT_{sec}} \propto \left[1 + \left(\frac{T_{sec}}{\Gamma}\right)^2\right]^{-1} \tag{6}$$

The value of Γ may in principle depend on the initial energy of the electron. However, by comparison with the data of Opal et al. [23] a constant value of 11.4 eV was found to be sufficient.

The emission angles of the primary and secondary electrons were chosen according to the suggestions given in Grosswendt and Waibel [14].

Results and checks

It is good practice to verify the predictions of MC calculations using experimental data on macroscopic quantities. Here W values and dose profiles are considered. We assume an electron point source at $z = 0$ emitting monoenergetic electrons along the positive z-axis.

W values. The W value is defined as the average energy needed to produce an electron-ion pair and includes the energy dissipated by electronic excitation. The W value is therefore sensitive to the ratio between the excitation and ionization cross sections. For most materials the W value ranges between 30 and 40 eV in the high energy limit. For large energies the W value is constant (≈ 30 eV in water vapor) due to the constant ratio of excitation to ionization cross sections. For lower energies it increases rapidly because of the steeply decreasing ionization cross section. In the vicinity of the ionization threshold a large fraction of the dissipated energy goes into electronic excitation rather than into ionization. Our MC calculation shows sufficient agreement, within 5%, with the measured data of Combecher [13].

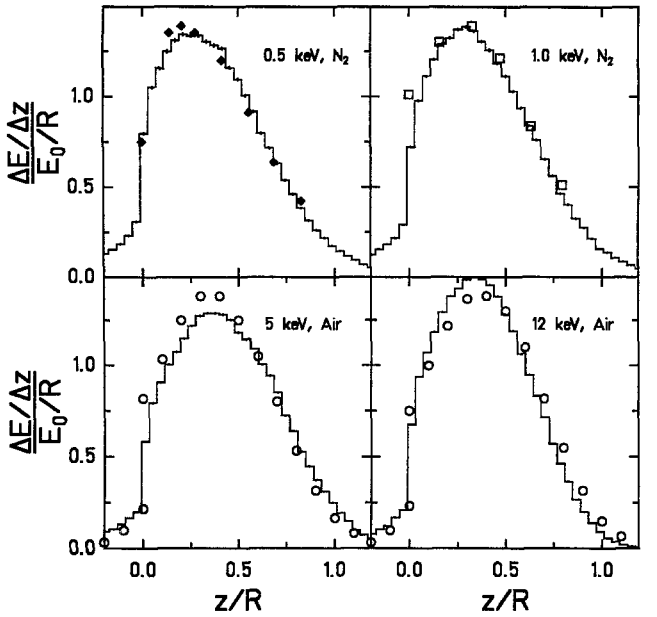

Fig. 3. Normalized axial dose profiles in low-Z materials. *Symbols*: experimental data for N_2 [3] and air [15]; *histograms*: calculations for H_2O, this work

Depth dose profiles

Figure 3 shows axial depth dose profiles for various materials. The experimental data [3, 15] were obtained by measuring the light emission profile originating from de-excitation via the 391.4-nm transition in N_2.

In the calculations for H_2O the total deposited energy dose for each z interval is summed up along the directions perpendicular to the z-axis. It is convenient to plot the results in the dimensionless quantity $(\Delta E/\Delta z)/(E_0/R_p)$ vs z/R_p, where R_p is the practical range and E_0 the incident kinetic energy. Then the profiles are widely independent of stopping material and incident electron energy. In Fig. 3, measurements and MC simulation results agree within 10%. It should be noted that the shapes of the profiles depend on the assumed R_p, defined with a precision not better than $\approx 5\%$.

Primary electron distributions

In this section the primary energy and angular distributions of electrons entering into the transport calculation will be discussed. In the present work the relatively simple theoretical approach of the binary encounter approximation (BEA) will be described and compared with experimental double-differential cross sections. Two classes of collision systems are distinguished: light and "structureless" projectiles, on the one hand, and heavy or structured projectiles, on the other. The processes of charge transfer into the continuum and projectile ionization are not included.

The binary encounter approximation

The BEA [8] is well suited to describe the secondary electron production by structureless projectiles such as protons or α particles.

The theory is essentially based on the assumption of a classic binary collision between a projectile with velocity v_p and a single target electron with initial velocity v_e. It yields basically the triple-differential cross section for the ejection of an electron at a polar angle θ with an energy transfer ΔE:

$$\frac{\mathrm{d}^3\sigma}{\mathrm{d}\Delta E\,\mathrm{d}\Omega\,\mathrm{d}v_e} = F(\Delta E, v_p, v_e, \theta) \tag{7}$$

An integration over the initial electron velocity distribution $f(v_e)$ is necessary to obtain the double-differential cross section:

$$\frac{\mathrm{d}^2\sigma}{\mathrm{d}\Delta E\,\mathrm{d}\Omega}(\Delta E, \theta) = \int_0^{v_{\max}} \frac{\mathrm{d}^3\sigma}{\mathrm{d}\Delta E\,\mathrm{d}\Omega\,\mathrm{d}v_e} f(v_e)\,\mathrm{d}v_e \tag{8}$$

where $v_{\max}$ is determined by kinematic constraints [8]. This integration is performed numerically. It was shown by Bonsen and Vriens [8] that, at least for light target atoms like He, it is sufficient to use a 1s hydrogenic distribution:

$$f(v_e) = n_{\text{shell}} \frac{32 v_e^2 v_0^5}{\pi (v_e^2 + v_0^2)^4} \tag{9}$$

where n_{shell} is the number of electrons in the shell under consideration. A reasonable choice of v_0^2 should give the average kinetic energy of the bound electrons according to the Virial theorem:

$$\langle E_{\text{kin}} \rangle = \tfrac{1}{2} m_e v_0^2 = -\tfrac{1}{2} \langle E_{\text{pot}} \rangle = R\left(\frac{Z - s_{nl}}{n}\right)^2 \tag{10}$$

where the rightmost expression follows the Slater rules [31]. The shielding constants s_{nl} depend on the shell number n and subshell number l. Although originally intended for use with atomic s shells only, in the present work the BEA formulas [Eqs. (7) and (9)] are applied to the water molecule. The five shells of H_2O are oxygen-like and have O1s, O2s, O2p, O2p, and O2p character [6, 30]. Thus, the application of the Slater rules yields $\langle E_{\text{kin}} \rangle = 806$, 70.4, 70.4, 70.4, and 70.4 eV.

Light and structureless projectiles

The light and structureless projectiles represent the class of collision systems for which the BEA is supposed to work best. Figure 4 shows experimental cross sections for 0.5 MeV protons on water vapor [32] compared with BEA calculations using different values of $\langle E_{\text{kin}} \rangle$. It is evident that the approach according to the Slater rules gives much better agreement with experimental data than the sometimes used alternative $\langle E_{\text{kin}} \rangle = E_{\text{bind}}$ with experimental binding energies E_{bind} (539.7, 32.2, 18.4, 14.7, and 12.6 eV; Ref. 30). For the spectrum at 15°

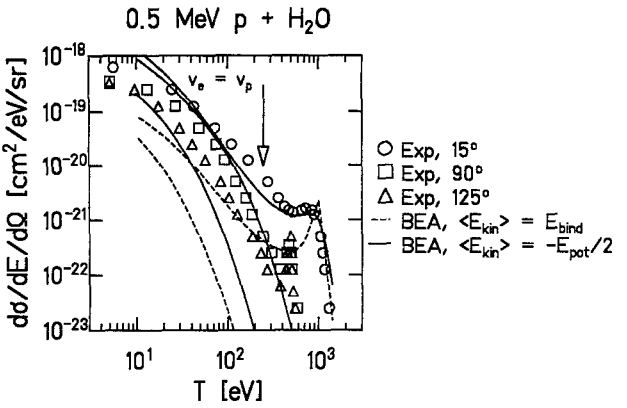

Fig. 4. Secondary electron energy spectra from the collision $p+H_2O$ at 0.5 MeV proton energy at various angles [32]. The curves are binary encounter approximation (BEA) calculations with various initial 1s velocity distributions. *Solid*: for 15°, 90°, and 125° emission angles with the mean kinetic energy according to the virial theorem and the Slater rules; *dashed*: for 15° and 125° emission angles with the mean kinetic energy equal to the experimental binding energy. The *arrow* indicates the electron energy corresponding to equal velocity of the projectile and ejected electrons

the classic binary peak is clearly visible at an energy of

$$T=4m_e\frac{E_{\text{proj}}}{M_{\text{proj}}}\cos^2\theta\approx 950\text{ eV}$$

The small angle spectra exhibit a contribution from continuum charge transfer at an energy where the projectile velocity equals that of the ejected electrons:

$$T=\frac{m_e}{m_p}T_p\approx 250\text{ eV}$$

The peak at ≈ 540 eV in the spectra at larger angles is due to Auger electrons which are emitted isotropically and therefore appear most pronounced at angles where δ-electron emission is less probable.

A major deficiency of the BEA theory is the underestimation of high-energy backward emission as one might expect from the classic binary collision approach. However, for energies >50 eV and the most important angular range $0<\theta<90°$, the agreement is quite good on an absolute scale.

Another comparison with experimental data concerning the angular distribution for selected energies is depicted in Fig. 5 for 1-MeV protons on water vapor. The discrepancy at backward angles $\theta>120°$ is evident. For angles $\theta<120°$ the quantitative agreement between experiment and BEA theory is good. The binary peak is especially well reproduced in width, height, and location. Only at the lowest energies, $T_{e^-}\ll 100$ eV, does the experiment show a virtually isotropic distribution due to the increasing contribution of larger ejection angles. The deviations in the forward direction $\cos\theta=1$ for 250–750 eV are caused by continuum charge transfer, expected to be centered around 500 eV. Figure 5 also shows similar data for the system $\alpha+H_2O$. The good agreement

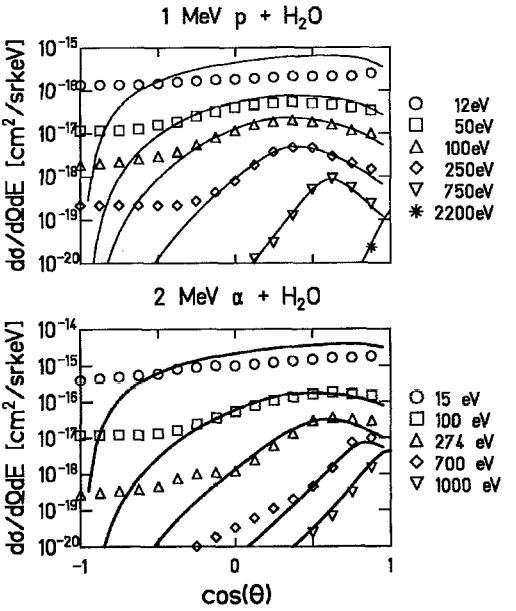

Fig. 5. Secondary electron angular distributions from the collision of 1-MeV protons [32], and 2-MeV α particles [33] on H_2O. The curves are BEA calculations with 1s velocity distributions according to the virial theorem and the Slater rules

between theory and experiment is due to the fact that the basic assumptions of the BEA are ideally fulfilled: an unstructured light ion hits a heavy target, ejecting electrons from an unperturbed electron cloud.

Heavy or structured projectiles

Collisions with heavy projectiles are normally beyond the scope of the BEA for several reasons.

- Due to the high charge of the projectile, the perturbation of the target electron cloud is not small.
- Projectile ionization may contribute to the cross section if the projectile is not fully stripped.
- The recoil effect on the target atom may be considerable.

An additional complication arises from a possible impact-parameter dependence of the effective projectile charge. In peripheral collisions corresponding to low electron energies the nuclear charge of a projectile is screened by the ion's remaining electrons, whereas in central collisions with high momentum transfer the target "sees" the full nuclear charge. This effect is most pronounced for ions which still carry many electrons, i.e., slow heavy ions.

In our calculations, where the heavy ion suffers many collisions, the projectile is assumed to have lost all electrons with $v_e < v_p$ so that projectile ionization is neglected. Therefore, the BEA will be used also for heavy projectiles due to its relative simplicity.

Data from the collision U^{33+} on Ne [17] are shown in Fig. 6 as an example. The calculations assume a projectile charge of $Z_{\text{eff}} = 33+$. The measured intensity is peaked strongly in the forward direction as a consequence of the kinematics of a collision between a very heavy projectile and a light target atom. This

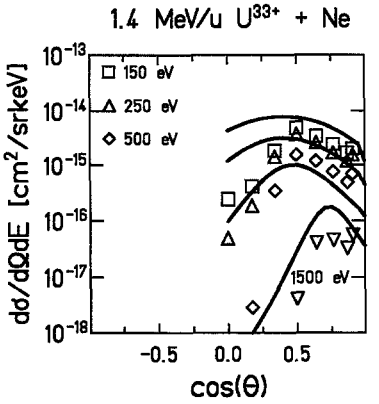

Fig. 6. Secondary electron angular distributions from the collision of a very heavy projectile with a light target at various electron energies [17]. The curves are BEA calculations

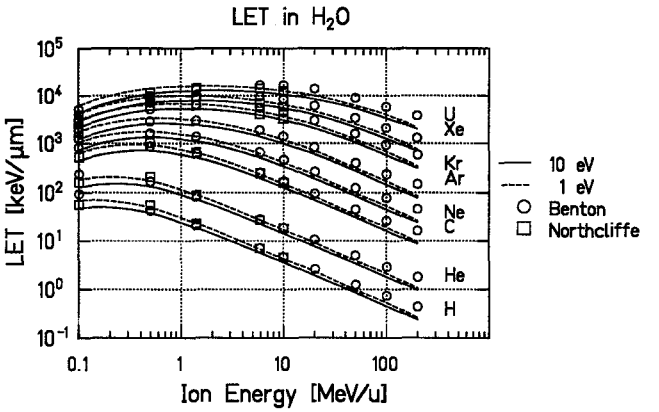

Fig. 7. Curves are linear energy transfer (LET) in water for various projectiles as a function of ion energy, computed with BEA. The *solid* and *dashed lines* correspond to lower electron energy thresholds of 10 and 1 eV, respectively. The values represented by the symbols are taken from tables in Refs. 4 and 22

behavior cannot be fully reproduced by the basic BEA calculation. It overestimates the yield toward backward angles. The agreement is surprisingly good at forward angles.

Computing the LET from the BEA

With the BEA one can calculate the electronic stopping power or LET by weighting the energy loss ΔE (including the binding energy) in a single collision with the differential cross section (8) and integrating numerically over the angle and kinetic energy of the ejected electrons. The projectile charge is calculated according to the formula of Barkas [2] in (11). The results are collected in Fig. 7 for some projectile-energy combinations with the minimum δ-electron energy as a parameter. Excitation of target molecules is neglected. Comparing the results with the tables in [4] and [22] one finds surprisingly good agreement

for all projectiles and ion energies below ≈ 100 MeV/u. The deviations increase with increasing ion energy, probably due to neglected relativistic effects in the BEA model.

Dose calculations

Calculation of dose proceeds as follows. A projectile moving along the z-axis interacts with the water molecules in the medium. The interaction points are sampled from an exponential distribution with a mean free path according to the total δ-electron emission cross section. Electrons are liberated from the molecules struck along the ion's path with energies and emission angles according to the double-differential cross section. The effective charge Z_{eff} for heavy projectiles with nuclear charge Z_0 is assumed following the formula of Barkas [2]:

$$Z_{\text{eff}} = Z_0 [1 - \exp(-125 \beta Z_0^{-\frac{2}{3}})] \tag{11}$$

with $\beta = v_p/c$. Charge equilibrium is supposed to be reached in the collisions within the first few micrograms per square centimeter [38].

The energy dissipated by the primary electrons and their secondaries during their deceleration is stored in a two-dimensional array $D(r^2, z)$, using cylindrical coordinates (r, z) to exploit the symmetry of the problem. To obtain the radial energy dose distribution $D_r(r)$ in grays, D is summed up along the z-coordinate and divided by the volume under consideration:

$$D_r(r)[\text{Gy}] = \frac{\Sigma_z D(r^2, z)[\text{keV cm}^{-3}]}{2\pi r \Delta r (z_{\max} - z_{\min}) \varrho N_{\text{ions}}} \times 1.602189 \times 10^{-13} \tag{12}$$

where ϱ is the bulk density and N_{ions} is the number of heavy projectiles considered. By default, the z-region for dose recording is limited by $z_{\min} = -R_p(E_{\max})$ and $z_{\max} = R_p(E_{\max})$. To avoid boundary effects the actual ion path is started at $2z_{\min}$ and stopped at $2z_{\max}$. The maximum electron energy $E_{\max}$ is chosen to be 1.5 times the binary peak at 0° for the BEA or the highest energy available from experimental input. Correspondingly, the minimum energy is taken as 10 eV or the lowest energy available from experimental input. The lower limit of r was fixed at $r = 10^{-8}$ cm to allow logarithmic representation for comparison with experiments. Inelastic events outside the limits of $D(r^2, z)$ are not recorded in the histogram but are still treated in the MC procedure. Thus, the total energy (including the binding energy) lost in the stopping material is equal to the LET. The calculated radial dose distributions, however, contain only the energy dissipated by the δ electrons. The scattering and energy loss of the primary ion is not accounted for in the current implementation. This simplification is justified for the simulation of usual ionization chamber measurements. For example, a 1-MeV proton with an energy loss of ≈ 250 MeV/gcm^{-2} loses ≈ 0.03 MeV on its path, $\Delta z = 4 R_p(E_{\max} = 3 \text{ keV}) = 12 \times 10^{-5}$ gcm^{-2}.

Experiments usually determine the radial dose distribution of a track by measuring the ionization current in a chamber filled with gas at low pressure. The spatial energy dose distribution is obtained by multiplying the measured currents with a constant W value. The distance in liquid water can be simulated by varying the gas pressure [40]. Therefore, an array $I(r^2, z)$ is provided to

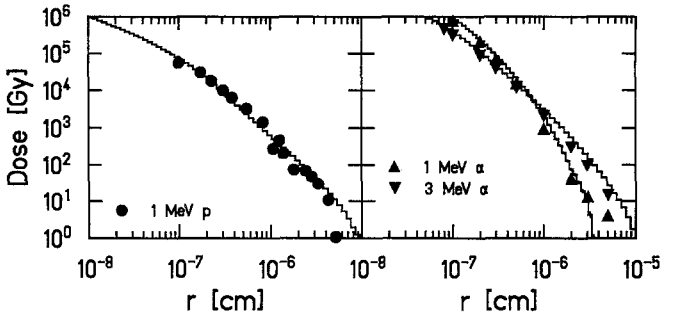

Fig. 8. Comparison of dose distributions for light projectiles of measured (*symbols*) [40] vs calculated (*histograms*) data

record the spatial distribution of ionization events. It is treated the same way as $D(r^2, z)$, but it must be multiplied with the same W value (in keV) as in the experiment for comparison with the measurements.

Light projectiles

Figure 8 shows radial dose profiles determined experimentally from ionization current measurements [40] compared with MC simulated distributions.

In general, the agreement of the BEA-based calculations with experiment is surprisingly good despite the deficiencies of the BEA angular distributions, due to the fact that the dose distribution at distances of a few nanometers is most affected by the cross section at $\theta = 90°$ for electron energies on the order of 100 eV. In this region, the agreement between experiment and the BEA theory is quite good. At very large distances the electrons in the binary peak are the most important. These are also well described by the theory.

The α-particle data show the general trend: as the ion energy increases, the dose distributions become flatter due to the increasing number of high-energy electrons that deposit an increasing fraction of their energy farther away from the ion path.

Medium-heavy projectiles

As examples of structured and medium-heavy projectiles, 2.57 MeV/u oxygen [37], 0.4 MeV/u bromine [38], and 17.2 MeV/u germanium ions [34], in tissue-equivalent gas (O, Br) and propane (Ge), respectively, are compared with calculations in water vapor of unit density. The primary double-differential cross sections are computed with the BEA using Barkas effective charges of 7.2, 10.1, and 29.0 for oxygen, bromine, and germanium, respectively. Figure 9 shows experimental and simulated radial doses for these systems. The oxygen data agree very well because the high effective charge of the projectile leaves it nearly unstructured. In contrast, the bromine system shows agreement only for short distances. This is probably the result of a distortion of the primary δ-electron spectrum due to screening effects. High-energy electrons are underestimated

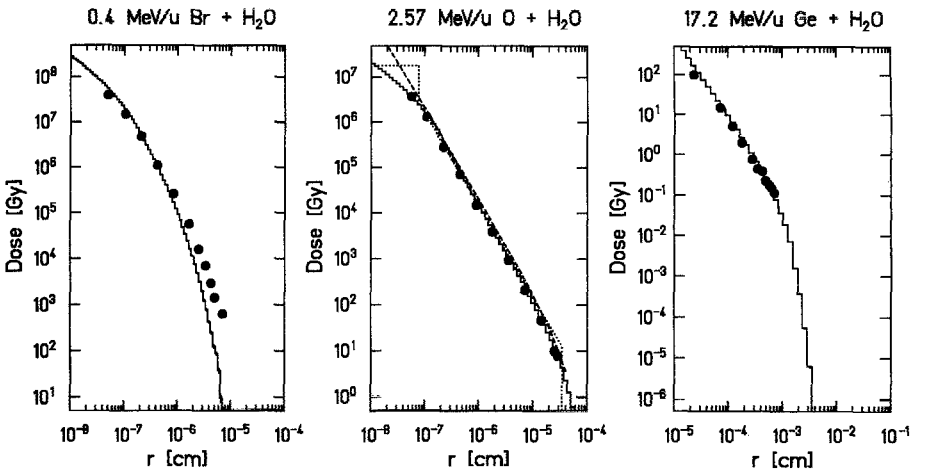

Fig. 9. Dose distributions measured (*symbols*) and simulated in water vapor of unit density (*histograms*) for various medium-heavy projectiles in tissue-equivalent gas (O, Br) and propane (Ge). For references see text. W values of 33.4 eV (O) and 36.7 eV (Br and Ge) were applied to convert ionization to dose distributions. The MC results for Ge were scaled with a factor of 2.5 to account for the different absolute height of the primary cross sections in water and propane. The additional curves for oxygen show the results according to the models of Butts and Katz (*dashed*; [9]) and Chatterjee and Holley (*dotted*; [10])

because they originate from close collisions where they see the full nuclear charge of the bromine projectile. This screening effect is relatively large for low-velocity bromine because it still carries the majority of its electrons.

The higher-energy germanium experiment is reproduced after scaling the MC results by a factor of 2.5 to account for the larger number of weakly bound electrons in propane compared with water. This is justified because it was shown experimentally [32] that the primary electron-emission cross sections for water and hydrocarbons are quite similar when normalized to the number of weakly bound electrons.

For the oxygen system the radial dose distributions according to the models of Butts and Katz [9] and Chatterjee and Holley [10] are shown. They are similar to the MC results for distances larger than 10^{-7} cm. Large differences can be found for smaller distances and also in the region of maximum range of the high energy δ electrons.

In Fig. 10 the validity of the model for high-energy projectiles is verified. At intermediate distances, the measured as well as the simulated doses show the usual r^{-2} dependence.

Very heavy projectiles

As pointed out previously, the BEA is not adequate to obtain the correct primary electron distribution for heavy projectiles. To demonstrate the effect on the radial dose, the experimental and theoretical distributions of Fig. 6 were used as input to the transport calculations in water. The resulting dose curves are compared in Fig. 11. They differ by a factor of 2–3. The rapid falloff at large

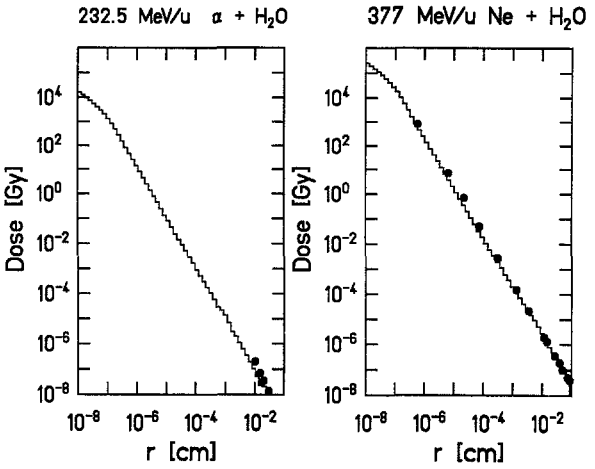

Fig. 10. Measured (*symbols*) and calculated (*histograms*) dose distributions for fast medium-heavy projectiles: 232 MeV/u α particles, data from Ref. 36; and 377 MeV/u Ne ions, data from Ref. 35, with $W = 33.7$ eV

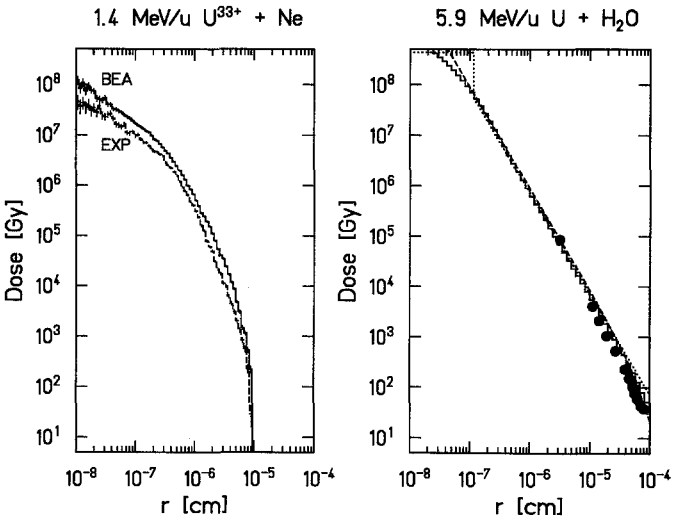

Fig. 11. Dose distributions for very heavy projectiles. For 1.4 MeV/u uranium: with the theoretical and experimental primary cross sections from Fig. 6, diffusion material was H_2O. For 5.9 MeV/u uranium: comparison of measured (*symbols*; Ref. 34) with calculated radial dose of uranium ions (*histograms*). The experiment was performed in propane, whereas the calculations assume H_2O as material. The results were scaled with a factor of 2.5 to account for the larger number of electrons in propane. The additional curves are calculations according to the models of Butts and Katz (*dashed*; [9]) and Chatterjee and Holley (*dotted*; [10])

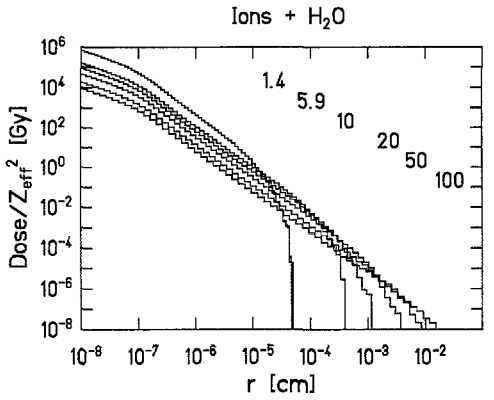

Fig. 12. Dose vs the distance from the ion's path. All curves are for protons on water, labeled with the projectile energy in MeV. A W value of 30 eV was assumed. The curves for other projectiles can be obtained by scaling with the values for the effective charge according to (11)

distances is artificial due to the limited range (< 1.5 keV) of the primary distributions in Fig. 6. The agreement is still quite reasonable, if the deficiencies of the BEA are kept in mind.

Figure 11 also shows dose distributions from 5.9 MeV/u uranium ions. The measurements were performed in propane, whereas the calculations use H_2O as material. Again, a factor of 2.5 was applied to account for the number of electrons in propane. In the range where data are available, experimental data and our MC calculation agree within a factor of 2.

The comparison with calculations according to the models of Butts and Katz [9] and Chatterjee and Holley [10] show the same differences as in the case of oxygen projectiles.

Radial dose systematics

In order to simplify comparisons between different projectile-energy combinations as well as to condense the representations, it is advantageous to establish systematics for the radial dose curves. The basic cross section [Eq. (7)] is practically independent of the projectile mass due to the negligible ratio of electron to projectile mass m_e/m_p. Hence, the spectral shape depends only on the projectile velocity being proportional to the square root of the energy per nucleon. The absolute height of the cross section is determined by the square of the effective charge also dependent on the projectile velocity and the nuclear charge Z_0 of the projectile. Therefore, the cross section and the dose curves derived from it can be parameterized as a product of two functions, $Z_{\text{eff}}^2(v_p, Z_0)$ and $f(v_p)$. This means that it is sufficient to calculate dose curves for protons with various energies to obtain the shape, and to multiply these curves by the square of the effective charge to obtain the absolute height. The results are shown in Fig. 12. The distributions obtained this way are quite similar out to large distances, where they fall of rapidly due to the finite range of the electrons ejected with the maximum energy possible in a binary collision.

Mean specific energy deposition in small sites

In addition to the computation of radial dose distributions, our code is capable of calculating the mean specific energy $\bar{z}_b$ deposited by ions in small sites. In

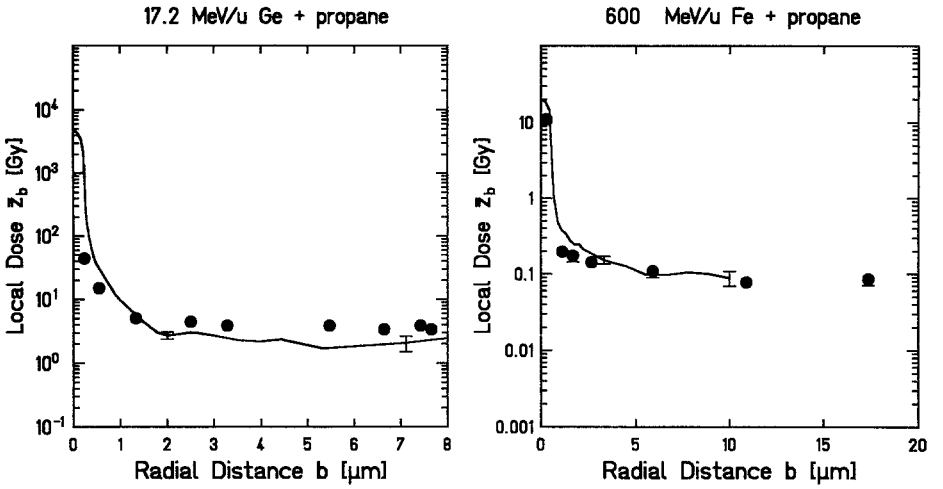

Fig. 13. Experimental (*symbols*) and simulated (*curves*) values for the mean specific energy deposited in small sites at various distances. *Left-hand side*, 17.2 MeV/u of Ge in 0.5-μm diameter sites [34]; *right-hand side*, 600 MeV/u of Fe in 1.3-μm diameter sites [20]

contrast to the dose, which is an average over all events, $\bar{z}_b$ is obtained event by event. The experiments reported in Toburen et al. [34] were simulated using a spherical site with a diameter of 0.5 μm. Experimental and simulation results for 17.2 MeV/u of germanium are shown in Fig. 13. At small distances the data are overestimated by our calculations due to the overestimation of the primary cross section for low δ-electron energies. The sharp rise in energy deposition toward $r=0$ is an artifact due to the finite size of the counting volume. At large distances the flattening of the experimental data caused by the high energy δ-electrons is reproduced within a factor of 1.5. One should note, however, that the experimental values at large distances have large systematic uncertainties due to the small signals of the detector which made them sensitive to noise. A high cutoff threshold in the energy spectra leads to a systematic overestimation of $\bar{z}_b$. Figure 13 shows, in addition, a comparison with data taken under better experimental conditions [20] with a 600-MeV/u iron beam. Again, the far-reaching δ-electron component can be reproduced. The overall agreement of the simulations with the measurements is better than in the germanium experiment.

Conclusion

The calculated radial dose distributions presented here are in good agreement with all published experiments. This is a surprising result when the shortcomings of the BEA theory and the complexity of the electron emission (as summarized, e.g., in Ref. 27) are realized. Models using a physically less-justified angular and energy distribution are also able to characterize the radial dose distribution with reasonable accuracy. The main feature of all calculations is the r^{-2} dependence of the radial dose. This dependence is also predicted in the track structure model of Butz and Katz [9] and in the core-penumbra model of Chatterjee

and Schaefer [11]. However, in contrast to the core-penumbra model our calculations do not exhibit a central region of elevated energy deposition. The radial dose rises as r^{-2} decreases, down to distances around 1 nm. At smaller distances the increase is less steep. Measurements of the radial dose around alpha particle tracks by Colautti et al. [12] show a similar trend. It should be noted, however, that the inner part of a track is the most sensitive region when the BEA is replaced by more realistic initial electron distributions for very heavy ions. Because the BEA generally overestimates low-energy electrons, such a replacement would rather yield a dose reduction in the inner part of the track.

Solid-state effects, such as recombination of the low-energy electrons with the positive deficiencies, would also reduce the biologically relevant dose in the inner region. The same amount of energy is dissipated in more reaction channels, a finding which does not necessarily lead to biological damage.

Recently, a parameter-free track structure model [28] was used to calculate the cell inactivation probability of heavy ions on the basis of the radial dose distribution and the measured X-ray sensitivity, without assuming different interaction modes of high and low LET radiation. The success of this model in reproducing the measured data on the basis of an r^{-2}-radial dose distribution gives some confidence that no dramatic change is expected when solid-state effects in the central track region are included. However, the unique biological effects of particle radiation should not be attributed to the action of a restricted high LET area accompanied by a few δ electrons. Instead, the high LET effects of the charged particles have to be attributed to the spatial pattern of the primary ionization and to the ionization caused by the subsequent electron diffusion.

References

1. Aufderheide E, Rink H, Hieber I, Kraft G (1985) Heavy ion effects on cellular DNA: strand break induction and repair. Int J Radiat Biol 5:779–790
2. Barkas WH (1963) Nuclear research emulsions (vol 1). Academic Press, New York
3. Barrett JL, Hays PB (1976) Spatial distribution of energy deposited in nitrogen by electrons. J Chem Phys 64(2):743–750
4. Benton EV (1968) Study of charged particle tracks in cellulose nitrate. US Naval Radiologic Defense Laboratory TR 68-14
5. Berger MJ (1963) Monte Carlo calculation of the penetration and diffusion of fast charged particles. Methods Comp Phys 1:135–215
6. Berkowitz J (1979) Photoabsorption, photoionization, and photoelectron spectroscopy. Academic Press, New York
7. Bethe HA (1930) Zur Theorie des Durchganges schneller Korpuskularstrahlen durch Materie. Ann Phys (Leipzig) 5:325–400
8. Bonsen TF, Vriens L (1970) Angular distribution of electrons ejected by charged particles. Physica 47:307–319
9. Butts JJ, Katz R (1967) Theory of RBE for heavy ion bombardment of dry enzymes and viruses. Radiat Res 30:855–871
10. Chatterjee A, Holley WR (1991) Energy deposition mechanisms and biochemical aspects of DNA strand breaks by ionizing radiation. Int J Quant Chem 39:709–727
11. Chatterjee A, Schaefer HJ (1976) Microdosimetric structure of heavy ion tracks in tissue. Radiat Environ Biophys 13:215–227
12. Colautti P, Talp G, Tornielli G (1992) Measurements of ionization distributions at nonometre level. In: Chadwick KH, Moschini G, Varma MN (eds) Biophysical modelling or radiation effects. Adam Hilger, Brussels, pp 269–276
13. Combecher D (1980) Measurement of W values of low-energy electrons in several gases. Radiat Res 84:189–218
14. Grosswendt B, Waibel E (1978) Transport of low energy electrons in nitrogen and air. Nucl Instrum Methods 155:145–156

15. Grün AE (1957) Lumineszenz-photometrische Messungen der Energieabsorption im Strahlungsfeld von Electronenquellen. Z Naturforsch 12a:89–95
16. Heilmann J, Rink H, Taucher-Scholz G, Kraft G (1993) DNA strand break induction and rejoining and cellular recovery in mammalian cells after heavy-ion irradiation. Radiat Res 135:46–55
17. Kelbch CH, Olson RE, Schmidt S, Schmidt-Böcking H, Hagmann S (1989) Unexpected angular distribution of the δ-electron emission in 1.4 MeV/u U^{33+} rare gas collisions. J Phys B 22:2171–2178
18. Kieffer L (1971) Low-energy electron-collision cross-section data. Atomic Data 2:293
19. Kraft G (1987) Radiobiological effects of very heavy ions. Nucl Sci Appl 3:1–28
20. Metting NF, Rossi HH, Braby LA, Kliauga PJ, Howard J, Zaider M, Schimmerling W, Wong M, Rapkin M (1988) Microdosimetry near the trajectory of high-energy heavy ions. Radiat Res 116:183–195
21. Moliere G (1948) Theorie der Streuung schneller geladener Teilchen. Z Naturforsch 3a:78–97
22. Northcliffe LC, Schilling RF (1970) Range and stopping-power tables for heavy ions. Nucl Data Tables A7:233
23. Opal JB, Beaty EC, Peterson WK (1972) Tables of secondary-electron-production cross sections. Atomic Data 4:209–253
24. Paretzke HG (1988) Simulation von Elektronenspuren im Energiebereich 0.01–10 keV in Wasserdampf. GSF-Forschungszentrum für Umwelt und Gesundheit, Bericht 24/88
25. Paretzke HG, Berger MJ (1978) Stopping power and energy degradation for electrons in water vapor. In: Booz J, Ebert HG (eds) Proceedings of the 6th symposium on microdosimetry. Harwood, Brussels, pp 749–758
26. Rossi HH (1968) Microscopic energy distribution in irradiated matter. In: Attix FH, Roesch WC (eds) Radiation dosimetry (vol 1). Academic Press, New York, pp 43–92
27. Schmidt-Boecking H, Ramm U, Kraft G, Ullrich J, Berg H, Kelbch C, Olson RE, Dubois R, Hagmann S, Jiazhen F (1992) δ-Electron emission in fast heavy ion-atom collisions. Adv Space Res 12:7–15
28. Scholz M, Kraft G (1992) A parameter-free track structure model for heavy ion action cross section. In: Chadwick KH, Moschini G, Varma MN (eds) Biophysical modelling of radiation effects. Adam Hilger, Brussels, pp 185–192
29. Schutten, J, deHeer FJ, Moustafa HR, Boerboom AJH, Kistemaker J (1966) Gross- and partial-ionization cross sections for electrons on water vapor in the energy range 0.1–20 keV. J Chem Phys 44(10):3924–3928
30. Siegbahn K Nordling C, Johannson G, Hedman J, Hedén PF, Humrin K, Gelius U, Bergmark T, Werme LO, Manne R, Baer Y (1971) ESCA applied to free molecules. North Holland, Amsterdam, pp 82–85
31. Slater JC (1960) Quantum theory of atomic structure (vol 1). McGraw-Hill, New York
32. Toburen LH, Wilson WE (1977) Energy and angular distributions of electrons ejected from water vapor by 0.3–1.5 MeV protons. J Chem Phys 66(11):5202–5213
33. Toburen LH, Wilson WE, Popovich RJ (1980) Secondary electron emission from ionization of water vapor by 0.3- to 2.0-MeV He^+ and He^{2+} ions. Radiat Res 82:27–44
34. Toburen LH, Braby LA, Metting NF, Kraft G, Scholz M, Kraske F, Schmidt-Böcking H, Dörner R, Seip R (1990) Radial distributions of energy deposited along charged particle tracks. Radiat Prot Dosimetry 31(1/4):199–203
35. Varma MN, Baum JW (1980) Energy deposition in nanometer regions by 377 MeV/Nucleon ^{20}Ne ions. Radiat Res 81:355–363
36. Varma MN, Paretzke HG, Baum JW, Lyman JT, Howard J (1976) Dose as a function of radial distance from a 930 MeV ^4He ion beam. In: Booz J, Ebert HG, Smith BGR (eds) Proceedings of the 5th symposium on microdosimetry. Luxembourg, Commission of the European Communities, pp 75–95
37. Varma MN, Baum JW, Kuehner AV (1977) Radial dose, LET, and W for ^{16}O ions in N_2 and tissue-equivalent gases. Radiat Res 70:511–518
38. Varma MN, Baum JW, Kuehner AV (1980) Stopping power and radial dose distribution for 42 MeV bromine ions. Phys Med Biol 25/4:651–656
39. Trajmar S, Register DF, Chutjian A (1983) Electron scattering by molecules. II. Experimental methods and data. Phys. Rep 97/5:219–356
40. Wingate CL, Baum JW (1976) Measured radial distributions of dose and LET for alpha and proton beams in hydrogen and tissue-equivalent gas. Radiat Res 65:1–19